AIAA JOURNAL
Vol. 47, No. 6, June 2009

Implicit Weighted Essentially Nonoscillatory Schemes with Antidiffusive Flux for Compressible Viscous Flows

Jaw-Yen Yang,* Tsang-Jen Hsieh, and Ching-Hua Wang
National Taiwan University, Taipei 10606, Taiwan, Republic of China

DOI: 10.2514/1.38148

A class of lower–upper symmetric-Gauss–Seidel, implicit, antidiffusive, weighted essentially nonoscillatory schemes for solving the two- and three-dimensional compressible Navier–Stokes equations with the Spalart–Allmaras one-equation turbulence model is presented. A weighted essentially nonoscillatory spatial operator with and without antidiffusive flux is employed for inviscid fluxes and central differencing for viscous fluxes. A numerical flux of weighted essentially nonoscillatory scheme in flux-limiter form is adopted, which consists of first-order and high-order fluxes and allows for a more flexible choice of first-order dissipative methods. The computations are performed for the two-dimensional turbulent flows over NACA 0012 and RAE 2822 airfoils and the three-dimensional turbulent flow over an ONERA M6 wing. By using the weighted essentially nonoscillatory scheme with antidiffusive flux corrections, the present solutions indicate that better resolution of contact discontinuities related flow structures and the convergence rate for steady-state computation are good, as compared with that using the original fifth-order weighted essentially nonoscillatory scheme combined with the Roe scheme on the same meshes. The present solutions are also compared with experimental data and other computational results and exhibit good agreement.

Nomenclature

$\hat{A}, \hat{B}, \hat{C}$	=	Jacobian matrices
a	=	speed of sound
d	=	distance from the wall
E, F, G	=	Cartesian components of the convective flux vector
E_v, F_v, G_v	=	Cartesian components of the viscous flux vector
$\hat{E}$	=	physical flux
$\tilde{E}$	=	numerical flux
$\tilde{E}^{HW}$	=	higher-order numerical flux
$\tilde{E}^{L}$	=	first-order numerical flux
e	=	energy per unity volume
H	=	source state vector
IS	=	smoothness indicators
J	=	Jacobian of coordinates transformation
K_l, K_t	=	laminar and turbulent thermal conductivity
L	=	characteristic length
l_s	=	left eigenvectors of Jacobian matrices
$\mathbf{n}$	=	unit normal vector
Pr	=	Prandtl number
p	=	pressure
Q	=	state vector of conserved variables
q	=	heat flux
Re	=	Reynolds number
r_s	=	right eigenvectors of Jacobian matrices
$\mathbf{S}^{\xi}$	=	surface area vector in the ξ direction
t	=	time
u, v, w	=	Cartesian components of the velocity vector
γ	=	specific heat ratio
$\delta_\xi, \delta_\eta, \delta_\zeta$	=	difference operators with respect to ξ, η, ς
μ	=	molecular viscosity
μ_l, μ_t	=	laminar and turbulent viscosity
ξ, η, ς	=	body-fitted curvilinear coordinates
ρ	=	density
τ_{ij}	=	viscous stress tensor
$\tilde{\upsilon}$	=	nondimensional eddy viscosity
φ_i	=	discontinuity indicator

Subscripts

i, j, k	=	grid-point index of variables
υ	=	viscosity variable
∞	=	freestream value

I. Introduction

THE essentially nonoscillatory (ENO) schemes developed by Harten et al. [1] are uniformly high-order-accurate right up to discontinuities, while keeping a sharp, essentially nonoscillatory, shock transition. Later, Shu and Osher [2,3] devised an efficient flux version. Since then, ENO schemes have been successfully applied to many different fields, as listed by Cockburn et al. [4]. However, they also have certain drawbacks. One of the main problems for aerodynamic flow computations is that the convergence rate of steady-state calculation using the implicit ENO scheme is generally poor and becomes stagnant without convergence. On the other hand, implicit total-variation-diminishing (TVD) schemes [5] as constructed out of Harten's TVD scheme [6] can achieve good convergence property. Rogerson and Meiburg [7] found that the numerical solutions of ENO schemes, as originally proposed by Harten et al. [1], do not always converge uniformly. Shu [8] proposed a modified ENO scheme, which recovers the correct order of accuracy for the test problem. A comparison of finite volume and finite difference implementation of high-order-accurate ENO schemes were given by Casper et al. [9].

The weighted ENO (WENO) schemes proposed by Liu et al. [10] and extended by Jiang and Shu [11] can overcome the drawbacks of ENO methods, as reported in [7], while keeping their robustness and high-order accuracy. The primary concept of WENO schemes is that instead of using only one of the candidate stencils based on divided difference to form the reconstruction, one uses a convex combination of all the candidate stencils. Each of the candidate stencils is assigned a weight that determines the appropriate contribution of this stencil to the final approximation of the numerical flux. A class of implicit

Received 21 April 2008; revision received 22 October 2008; accepted for publication 27 January 2009.

*Institute of Applied Mechanics; yangjy@spring.iam.ntu.edu.tw. Member AIAA (Corresponding Author).

WENO schemes has been successfully applied to incompressible and compressible flow problems by Chen et al. [12], Yang et al. [13], Perng et al. [14], and Yang et al. [15]. Good convergence rate to steady-state solution has been illustrated.

In recent years, several variants and improvements of the original WENO schemes [11] have been proposed [16–20]. By introducing an antidiffusive flux, Despres and Lagoutiere [16] proposed a first-order approach called the limited downwind scheme to prevent the smearing of contact discontinuities while keeping nonlinear stability. Bouchut [17] later modified this scheme to satisfy entropy conditions and also gave a simple explicit formula for this limited downwind antidiffusive flux. As inspired by these works [16,17], Xu and Shu [18] developed an antidiffusive flux correction technique based on a high-order finite difference WENO scheme, and the resulting scheme maintains high-order accuracy in smooth regions, nonoscillatory behavior near discontinuities, and sharp contact-discontinuity resolution. A mapped WENO scheme has been devised by Henrick et al. [19] that improves over the original WENO scheme at critical points. Zhang and Shu [20] suggested a modified smoothness indicator for the fifth-order WENO scheme (WENO5) near a steady shock region, and they showed that the residue for the WENO scheme with the new smoothness indicator can converge to machine zero for one- and two-dimensional steady problems with strong shock waves when there is no influence from the boundary conditions.

In this paper, following [14,15,18–20], an implicit version of the weighted essentially nonoscillatory scheme with antidiffusive flux is adopted for the two- and three-dimensional compressible Navier–Stokes equations for computing steady-state flows. A numerical flux of a WENO scheme in flux-limiter form is presented, which consists of first-order and high-order fluxes and allows for a more flexible choice of first-order entropy-satisfying dissipative methods. Several first-order dissipative schemes can be used [21]. This is an extension of previous work for the compressible Euler equations [22]. We aim at improving the resolution of contact discontinuities and their subsequent evolution and possible interaction with other flow structures such as shock waves and vortical flows. For turbulent flow calculations, Spalart–Allmaras a one-equation turbulence model [23,24] simplified by dropping the transition terms is adopted, which is based on the transport of eddy viscosity. The model provides a desirable tool for numerical computation of flow involving complex geometry. The performance of this model has been tested through comparison with experimental data of several well-documented flow cases. We apply the resulting implicit WENO schemes with antidiffusive flux to compute standard transonic viscous flows over NACA 0012 and RAE 2822 airfoils and three-dimensional transonic viscous flow over an ONERA M6 wing to test both the convergence rate and the accuracy of the methods.

II. Governing Equations

The governing equations are the unsteady Reynolds averaged compressible Navier–Stokes equations, which express the conservations of mass, momentum, and energy for a viscous gas. The Spalart–Allmaras one-equation turbulence model as devised in [23,24] is adopted. In the Cartesian coordinates, the three-dimensional governing equations are given by

$$\frac{\partial Q}{\partial t}+\frac{\partial E}{\partial x}+\frac{\partial F}{\partial y}+\frac{\partial G}{\partial z}=\frac{\partial E_v}{\partial x}+\frac{\partial F_v}{\partial y}+\frac{\partial G_v}{\partial z}+H \tag{1}$$

where

$$\begin{aligned} Q&=(\rho,\rho u,\rho v,\rho w,e,\tilde{\nu})^T\\ E&=(\rho u,\rho u^2+p,\rho uv,\rho uw,(e+p)u,\tilde{\nu}u)^T\\ F&=(\rho v,\rho vu,\rho v^2+p,\rho vw,(e+p)v,\tilde{\nu}v)^T\\ G&=(\rho w,\rho wu,\rho wv,\rho w^2+p,(e+p)w,\tilde{\nu}w)^T \end{aligned} \tag{2}$$

$$\begin{aligned} E_v&=\frac{1}{Re_\infty}\left(0,\tau_{xx},\tau_{xy},\tau_{xz},E_{v5},f_{v6}\frac{\partial\tilde{\nu}}{\partial x}\right)^T\\ F_v&=\frac{1}{Re_\infty}\left(0,\tau_{xy},\tau_{yy},\tau_{yz},F_{v5},f_{v6}\frac{\partial\tilde{\nu}}{\partial y}\right)^T\\ G_v&=\frac{1}{Re_\infty}\left(0,\tau_{xz},\tau_{yz},\tau_{zz},G_{v5},f_{v6}\frac{\partial\tilde{\nu}}{\partial z}\right)^T \end{aligned} \tag{3}$$

with

$$\begin{aligned} E_{v5}&=u\tau_{xx}+v\tau_{xy}+w\tau_{xz}-q_x\\ F_{v5}&=u\tau_{xy}+v\tau_{yy}+w\tau_{yz}-q_y\\ G_{v5}&=u\tau_{xz}+v\tau_{yz}+w\tau_{zz}-q_z\\ H&=(0,0,0,0,0,H_6)^T \end{aligned}$$

and

$$f_{v6}=\frac{1}{\sigma_\varepsilon}\left(\frac{\mu_l}{\rho}+(1+C_{B2})\tilde{\nu}\right)$$

In the preceding equations, ρ is the density; u, v, and w are the velocity components; e is the energy per unit volume; and $\tilde{\nu}$ is the turbulent variable, defined subsequently. The pressure p is related to other flow variables by the equation of state for a perfect gas:

$$p=(\gamma-1)[e-\rho(u^2+v^2+w^2)/2] \tag{4}$$

where γ is the ratio of specific heats. The heat flux terms are given by

$$q_j=-(K_l+K_t)\frac{\partial T}{\partial x_j}\qquad j=1,2,3 \tag{5}$$

$$K_l=\frac{\mu_l}{(\gamma-1)M_\infty^2 Pr_l}\qquad K_t=\frac{\mu_t}{(\gamma-1)M_\infty^2 Pr_t}$$

where $Pr_l=0.72$ and $Pr_t=0.9$ for air. The viscous stress tensors are obtained from

$$\tau_{ij}=(\mu_l+\mu_t)\left(S_{ij}-\frac{1}{3}\frac{\partial u_k}{\partial x_k}\delta_{ij}\right) \tag{6}$$

$$S_{ij}=\frac{1}{2}\left(\frac{\partial u_i}{\partial x_j}+\frac{\partial u_j}{\partial x_i}\right) \tag{7}$$

where i, $j=1$, 2, 3 indicate the three coordinate directions. The molecular viscosity μ_l is calculated by Sutherland's law.

The Spalart–Allmaras model is an eddy-viscosity model based on a transport equation for turbulent viscosity. The model was devised to improve the predictions obtained with algebraic mixing-length models, to develop a local model for complex flows, and to provide a simpler alternative to two-equation turbulence models. The eddy-viscosity function is defined in terms of a nondimensional eddy-viscosity variable $\tilde{\nu}$ and a wall damping function f_{v1}, as follows:

$$\nu_t=\rho\tilde{\nu}f_{v1}$$

The nondimensional convective transport equation of the eddy-viscosity is modeled as

$$\begin{aligned} \frac{\partial\tilde{\nu}}{\partial t}+\frac{\partial\tilde{\nu}u_j}{\partial x_j}&=C_{b1}(1-f_{t2})S\tilde{\nu}+\frac{1}{Re_\infty\sigma_\varepsilon}\left[\frac{\partial}{\partial x_j}\left((\nu+\tilde{\nu})\frac{\partial\nu}{\partial x_j}\right)\right.\\ &\left.+C_{b2}\frac{\partial\tilde{\nu}}{\partial x_j}\frac{\partial\tilde{\nu}}{\partial x_j}\right]-\frac{C_{w1}f_w}{Re_\infty}\left(\frac{\tilde{\nu}}{d}\right)^2+\frac{C_{b1}f_{t2}}{Re_\infty}d\left(\frac{\tilde{\nu}}{d}\right)^2+\frac{1}{Re_\infty}f_{t1}\Delta U^2 \end{aligned} \tag{8}$$

where the terms in the right-hand side (RHS) of the preceding equation represent turbulence eddy-viscosity production, conservative diffusion, nonconservative diffusion, near-wall turbulence

destruction, transition damping of production, and transition source of turbulence. The functions to control the laminar region of the shear layer and transition to turbulence are defined with function f_{t1} and f_{t2} to control the transition damping of production and transition source of turbulence, respectively. Because the location of the transition is not predetermined and the prediction of trip (start of transition) is out of the scope of this paper, we neglect the effects of transition model and focus on the validated case of laminar or fully turbulent conditions. The last two terms of Eq. (8) are omitted. In present study, we formulate the convective transport equation of the eddy viscosity in the form with a convective term, dissipative term as in Eqs. (1) and (2), and source term, which is expressed as

$$H_6 = C_{b2}(1-f_{t2})\Omega\tilde{\nu} + \frac{1}{Re_\infty}\left(\frac{C_{b1}f_{v2}}{k^2} - C_{w1}f_w\right)\left(\frac{\tilde{\nu}}{d}\right)^2 + \frac{1}{Re_\infty}\left(\frac{C_{b2}\tilde{\nu}}{\sigma_\varepsilon}\right)\nabla^2\tilde{\nu} \tag{9}$$

The model constants and auxiliary functions as devised in [25] are adopted. The basic model constants for free-shear flow to control the production and diffusion of turbulent eddy viscosity in the boundary-layer zone are

$$C_{b1} = 0.1366 \qquad C_{b2} = 0.622 \qquad \sigma_\varepsilon = 2/3$$

The additional model constants and auxiliary functions for the destruction of turbulent eddy viscosity in the boundary-layer zone are

$$C_{w1} = \frac{C_{b1}}{\kappa^2} + \frac{1+C_{b2}}{\sigma_\varepsilon} \qquad C_{w2} = 0.3 \qquad C_{w3} = 2$$

$$r = \frac{\tilde{\nu}}{Re_\infty S\kappa^2 d^2} \qquad g = r + C_{w2}(r^6 - r)$$

$$f_w = g\left(\frac{1+C_{w3}^6}{g^6 + C_{w3}^6}\right)^{1/6}$$

For the near-wall flow regions, the functions and constants are given by

$$S = \Omega + \frac{\tilde{\nu}f_{v2}}{Re_\infty\kappa^2 d^2}$$

$$\Omega = ((u_y - v_x)^2 + (v_z - w_y)^2 + (u_z - w_x)^2)^{0.5} \qquad \chi = \frac{\tilde{\nu}}{\nu_l}$$

$$f_{v2} = 1 - \frac{\chi}{1+\chi f_{v1}} \qquad f_{v1} = \frac{\chi^3}{(\chi^3 + C_{v1}^3)}$$

The model uses distance to the nearest wall, d, in its formulation and provides smooth laminar-turbulent transition capabilities.

The dimensional quantities (denoted by an overbar) are nondimensionalized using freestream conditions (denoted by subscript ∞) and characteristic length $\bar{L}$:

$$x = \frac{\bar{x}}{\bar{L}} \qquad y = \frac{\bar{y}}{\bar{L}} \qquad z = \frac{\bar{z}}{\bar{L}} \qquad t = \frac{\bar{t}\bar{V}_\infty}{\bar{L}} \qquad \rho = \frac{\bar{\rho}}{\bar{\rho}_\infty}$$

$$u = \frac{\bar{u}}{\bar{V}_\infty} \qquad v = \frac{\bar{v}}{\bar{V}_\infty} \qquad w = \frac{\bar{w}}{\bar{V}_\infty} \qquad a = \frac{\bar{a}}{\bar{a}_\infty} \qquad p = \frac{\bar{p}}{\bar{\rho}_\infty \bar{a}_\infty^2}$$

$$T = \frac{\bar{T}}{\bar{T}_\infty} \qquad \mu_l = \frac{\bar{\mu}_l}{\bar{\mu}_{l\infty}} \qquad \mu_t = \frac{\bar{\mu}_t}{\bar{\mu}_{l\infty}} \qquad \tilde{v} = \frac{\bar{\rho}\bar{\tilde{v}}}{\bar{\mu}_{l\infty}}$$

where $\bar{a}_\infty = (\gamma\bar{p}_\infty/\bar{\rho}_\infty)^{1/2}$ is the freestream speed of sound and $\bar{V}_\infty$ is the reference speed of freestream status.

To allow for the development of a discrete control volume formulation, Eq. (1) is presented in integral form:

$$\frac{\partial}{\partial t}\left(\frac{1}{V}\int_V Q\mathrm{d}V\right) + \frac{1}{V}\oint_\Omega (\Im - \Im_v)\cdot\mathbf{n}\mathrm{d}\Omega = \frac{1}{V}\int_V H\mathrm{d}V \tag{10}$$

$$\Im = E\mathbf{i} + F\mathbf{j} + G\mathbf{k} \qquad \Im_v = E_v\mathbf{i} + F_v\mathbf{j} + G_v\mathbf{k}$$

where V is the volume of the cell that is bounded by the surface Ω with the outward unit normal $\mathbf{n}$. We employed structured meshes, in which a generalized curvilinear coordinates system (ξ, η, and ζ) can be defined through a continuous transformation to the Cartesian coordinates x, y, and z. Each computational cell is defined by two ξ = constant, two η = constant, and two ζ = constant surfaces, respectively. The volume-averaged values for the conservative variables Q and the source terms H are defined as follows:

$$\bar{Q} = \frac{1}{V}\int_V Q\mathrm{d}V \qquad \bar{H} = \frac{1}{V}\int_V H\mathrm{d}V$$

Let $\mathbf{S}^\xi = \mathbf{n}^\xi S^\xi = S_x^\xi\mathbf{i} + S_y^\xi\,\mathbf{j} + S_z^\xi\,\mathbf{k}$ be the surface area vector in the ξ direction, then the fluxes at generalized coordinates (ξ, η, ζ) can be defined as

$$\hat{E} = \Im\cdot\mathbf{S}^\xi = (S_x^\xi E + S_y^\xi F + S_z^\xi G)$$

$$\hat{E}_v = \Im_v\cdot\mathbf{S}^\xi = (S_x^\xi E_v + S_y^\xi F_v + S_z^\xi G_v)$$

$$\hat{F} = \Im\cdot\mathbf{S}^\eta = (S_x^\eta E + S_y^\eta F + S_z^\eta G)$$

$$\hat{F}_v = \Im_v\cdot\mathbf{S}^\eta = (S_x^\eta E_v + S_y^\eta F_v + S_z^\eta G_v)$$

$$\hat{G} = \Im\cdot\mathbf{S}^\zeta = (S_x^\zeta E + S_y^\zeta F + S_z^\zeta G)$$

$$\hat{G}_v = \Im_v\cdot\mathbf{S}^\zeta = (S_x^\zeta E_v + S_y^\zeta F_v + S_z^\zeta G_v)$$

In the following, we associate the subscripts i, j, and k with the ξ, η, and ζ directions, and we use the half-integer subscripts to denote cell sides and the full integer subscripts to denote the cell itself or its centroid. Equation (10) may be expressed in semidiscrete conservation-law form, given by

$$\left(\frac{\partial\bar{Q}}{\partial t}\right)_{i,j,k} = -\frac{1}{V}[(\hat{E}-\hat{E}_v)_{i+1/2,j,k} - (\hat{E}-\hat{E}_v)_{i-1/2,j,k}] - \frac{1}{V}[(\hat{F}-\hat{F}_v)_{i,j+1/2,k} - (\hat{F}-\hat{F}_v)_{i,j-1/2,k}] - \frac{1}{V}[(\hat{G}-\hat{G}_v)_{i,j,k+1/2} - (\hat{G}-\hat{G}_v)_{i,j,k-1/2}] + \bar{H}_{i,j,k} \tag{11}$$

where

$$(\hat{E})_{i+1/2,j,k} = (\Im\cdot\mathbf{S}^\xi)_{i+1/2,j,k} = \hat{E}(Q_{i,j,k}, S_{i+1/2,j,k})$$

is the physical flux, evaluated based on the state variables at the cell center (i, j, and k) and the area vectors at the cell face ($i+1/2$, j, k). The rest of the fluxes at the cell faces can be similarly computed.

III. Numerical Methods and Boundary Conditions

A. Spatial Discretization

By dropping the averaged notation for convenience, a numerical approximation to Eq. (11) may be expressed in the form given by

$$\left(\frac{\partial Q}{\partial t}\right)_{i,j,k} = -\frac{1}{V}[(\tilde{E}-\tilde{E}_v)_{i+1/2,j,k} - (\tilde{E}-\tilde{E}_v)_{i-1/2,j,k}] - \frac{1}{V}[(\tilde{F}-\tilde{F}_v)_{i,j+1/2,k} - (\tilde{F}-\tilde{F}_v)_{i,j-1/2,k}] - \frac{1}{V}[(\tilde{G}-\tilde{G}_v)_{i,j,k+1/2} - (\tilde{G}-\tilde{G}_v)_{i,j,k-1/2}] + H_{i,j,k} \tag{12}$$

where $\tilde{E}$, $\tilde{F}$, and $\tilde{G}$ and $\tilde{E}_v$, $\tilde{F}_v$, and $\tilde{G}_v$ are, respectively, the numerical or representative inviscid and viscous fluxes at the bounding cell face for which discrete conservation is considered. Note that in the numerical framework given by Eq. (12), one needs to compute the cell volume and cell-face normal and the evaluations of the numerical fluxes $\tilde{E}$, $\tilde{F}$, and $\tilde{G}$ at cell sides involving cell-face normal (see [26,27]). The spatial differencing adopts weighted essentially nonoscillatory schemes [11] for the inviscid convective fluxes $\tilde{E}$, $\tilde{F}$,

and $\tilde{G}$ and adopts second-order central differencing for viscous fluxes $\tilde{E}_v$, $\tilde{F}_v$, and $\tilde{G}_v$. A WENO5 ($r = 3$) numerical flux at a cell surface $i + 1/2$ in direction i can be put into the form of a flux-limiter method and is defined by

$$\tilde{E}_{i+1/2,j,k} = \tilde{E}^{L}_{i+1/2,j,k} + \tilde{E}^{HW}_{i+1/2,j,k} \tag{13}$$

and

$$\tilde{E}^{\pm}_{i+1/2,j,k} = \tilde{E}^{L^{\pm}}_{i+1/2,j,k} + \tilde{E}^{HW^{\pm}}_{i+1/2,j,k}$$

where $\tilde{E}^{L}$ is the numerical flux of a first-order entropy-satisfying dissipative scheme and $\tilde{E}^{HW}$ is a high-order flux with WENO flux-limiter. Here, the Roe scheme with Harten's entropy fix [6] is adopted for the low-order numerical flux:

$$\tilde{E}^{L}_{i+1/2,j,k} = \tilde{E}^{L^{+}}_{i+1/2,j,k} + \tilde{E}^{L^{-}}_{i+1/2,j,k} \tag{14}$$

where

$$\tilde{E}^{L^{+}}_{i+1/2,j,k} = \tfrac{1}{2}[\hat{E}(Q_{i,j,k}, S_{i+1/2,j,k}) + (R|\Lambda|R^{-1})_{i+1/2,j,k} Q_{i,j,k}] \tag{15a}$$

$$\tilde{E}^{L^{-}}_{i+1/2,j,k} = \tfrac{1}{2}[\hat{E}(Q_{i+1,j,k}, S_{i+1/2,j,k}) - (R|\Lambda|R^{-1})_{i+1/2,j,k} Q_{i+1,j,k}] \tag{15b}$$

and $\hat{E}(Q_{i,j,k}, S_{i+1/2,j,k})$ is the physical flux, evaluated based on the state variables at the cell center (i, j, and k) and the area vectors at the cell face ($i + 1/2, j, k$), as described before. R is the similarity transformation matrix consisting of the right eigenvectors of the Euler system linearized around the Roe-averaged state between $Q_{i+1,j,k}$ and $Q_{i,j,k}$.

The $\tilde{E}^{HW}$ in Eq. (13) is a high-order flux and for ($r = 3$) WENO5, it is defined by

$$\tilde{E}^{HW}_{i+1/2,j,k} = \sum_{s=1}^{6} \tilde{E}^{HW}_{(i+1/2,j,k),s} \cdot r_s \tag{16}$$

with

$$\tilde{E}^{HW}_{(i+1/2,j,k),s} = \tilde{E}^{HW^{+}}_{(i+1/2,j,k),s} + \tilde{E}^{HW^{-}}_{(i+1/2,j,k),s} \tag{17}$$

where

$$\begin{aligned}
\tilde{E}^{HW^{+}}_{(i+1/2,j,k),s} &= \tfrac{1}{6}(\omega^{+}_{0,s} q^{+}_0 + \omega^{+}_{1,s} q^{+}_1 + \omega^{+}_{2,s} q^{+}_2) \\
\tilde{E}^{HW^{-}}_{(i+1/2,j,k),s} &= \tfrac{1}{6}(\omega^{-}_{0,s} q^{-}_0 + \omega^{-}_{1,s} q^{-}_1 + \omega^{-}_{2,s} q^{-}_2) \\
q^{+}_0 &= -2\Delta E^{+}_{(i-3/2,j,k),s} + 5\Delta E^{+}_{(i-1/2,j,k),s} \\
q^{+}_1 &= \Delta E^{+}_{(i-1/2,j,k),s} + 2\Delta E^{+}_{(i+1/2,j,k),s} \\
q^{+}_2 &= 4\Delta E^{+}_{(i+1/2,j,k),s} - \Delta E^{+}_{(i+3/2,j,k),s} \\
q^{-}_0 &= \Delta E^{-}_{(i-1/2,j,k),s} - 4\Delta E^{-}_{(i+1/2,j,k),s} \\
q^{-}_1 &= -2\Delta E^{-}_{(i+1/2,j,k),s} - \Delta E^{-}_{(i+3/2,j,k),s} \\
q^{-}_2 &= -5\Delta E^{-}_{(i+3/2,j,k),s} + 2\Delta E^{-}_{(i+5/2,j,k),s}
\end{aligned} \tag{18}$$

Here,

$$\Delta E^{\pm}_{(i+1/2,j,k),s} = l_s \cdot \Delta E^{\pm}_{i+1/2,j,k} \tag{19}$$

$$\Delta E^{+}_{i+1/2,j,k} = \hat{E}(Q_{i+1,j,k}, S_{i+1/2,j,k}) - \tilde{E}^{L}_{i+1/2,j,k} \tag{20a}$$

$$\Delta E^{-}_{i+1/2,j,k} = \tilde{E}^{L}_{i+1/2,j,k} - \hat{E}(Q_{i,j,k}, S_{i+1/2,j,k}) \tag{20b}$$

The weights $\omega^{\pm}$ are defined by

$$\omega^{\pm}_{k,s} = \frac{\alpha^{\pm}_{k,s}}{\alpha^{\pm}_{0,s} + \alpha^{\pm}_{1,s} + \alpha^{\pm}_{2,s}} \qquad k = 0, 1, 2 \tag{21}$$

where

$$\begin{aligned}
\alpha^{+}_{0,s} = \tfrac{1}{10}(\varepsilon + \mathrm{IS}^{+}_{0,s})^{-2} \qquad \alpha^{+}_{1,s} = \tfrac{6}{10}(\varepsilon + \mathrm{IS}^{+}_{1,s})^{-2} \\
\alpha^{+}_{2,s} = \tfrac{3}{10}(\varepsilon + \mathrm{IS}^{+}_{2,s})^{-2}
\end{aligned} \tag{22a}$$

$$\begin{aligned}
\alpha^{-}_{0,s} = \tfrac{3}{10}(\varepsilon + \mathrm{IS}^{-}_{0,s})^{-2} \qquad \alpha^{-}_{1,s} = \tfrac{6}{10}(\varepsilon + \mathrm{IS}^{-}_{1,s})^{-2} \\
\alpha^{-}_{2,s} = \tfrac{1}{10}(\varepsilon + \mathrm{IS}^{-}_{2,s})^{-2}
\end{aligned} \tag{22b}$$

Here, $\varepsilon = 10^{-10}$ and IS are the smoothness indicators, defined as

$$\begin{aligned}
\mathrm{IS}^{+}_{0,s} &= \tfrac{13}{12}(-\Delta E^{+}_{(i-3/2,j,k),s} + \Delta E^{+}_{(i-1/2,j,k),s})^2 \\
&\quad + \tfrac{1}{4}(-\Delta E^{+}_{(i-3/2,j,k),s} + 3\Delta E^{+}_{(i-1/2,j,k),s})^2 \\
\mathrm{IS}^{+}_{1,s} &= \tfrac{13}{12}(-\Delta E^{+}_{(i-1/2,j,k),s} + \Delta E^{+}_{(i+1/2,j,k),s})^2 \\
&\quad + \tfrac{1}{4}(-\Delta E^{+}_{(i-1/2,j,k),s} - \Delta E^{+}_{(i+1/2,j,k),s})^2 \\
\mathrm{IS}^{+}_{2,s} &= \tfrac{13}{12}(-\Delta E^{+}_{(i+1/2,j,k),s} + \Delta E^{+}_{(i+3/2,j,k),s})^2 \\
&\quad + \tfrac{1}{4}(-3\Delta E^{+}_{(i+1/2,j,k),s} + \Delta E^{+}_{(i+3/2,j,k),s})^2
\end{aligned} \tag{23a}$$

and similarly,

$$\begin{aligned}
\mathrm{IS}^{-}_{0,s} &= \tfrac{13}{12}(-\Delta E^{-}_{(i-1/2,j,k),s} + \Delta E^{-}_{(i+1/2,j,k),s})^2 \\
&\quad + \tfrac{1}{4}(-\Delta E^{-}_{(i-1/2,j,k),s} + 3\Delta E^{-}_{(i+1/2,j,k),s})^2 \\
\mathrm{IS}^{-}_{1,s} &= \tfrac{13}{12}(-\Delta E^{-}_{(i+1/2,j,k),s} + \Delta E^{-}_{(i+3/2,j,k),s})^2 \\
&\quad + \tfrac{1}{4}(-\Delta E^{-}_{(i+1/2,j,k),s} - 3\Delta E^{-}_{(i+3/2,j,k),s})^2 \\
\mathrm{IS}^{-}_{2,s} &= \tfrac{13}{12}(-\Delta E^{-}_{(i+3/2,j,k),s} + \Delta E^{-}_{(i+5/2,j,k),s})^2 \\
&\quad + \tfrac{1}{4}(-3\Delta E^{-}_{(i+3/2,j,k),s} + \Delta E^{-}_{(i+5/2,j,k),s})^2
\end{aligned} \tag{23b}$$

In the preceding, r_s (column vector) and l_s (row vector) are the sth right and left eigenvectors of the Jacobian matrices and they are evaluated using Roe averages. The r_s and l_s used in Eqs. (16) and (19), respectively, are evaluated consistently at the $i + 1/2$ interface.

B. Antidiffusive Flux Corrections for WENO Schemes

The purpose of the antidiffusive flux corrections is to improve the resolution of contact discontinuities without sacrificing the accuracy and stability of the original WENO scheme. Equation (13) can be written as antidiffusive numerical flux in the following form:

$$\begin{aligned}
\tilde{E}^{a}_{i+1/2,j,k} &= \tilde{E}^{L}_{i+1/2,j,k} + \tilde{E}^{HW}_{i+1/2,j,k} + \varphi_i \cdot \min \mathrm{mod} \\
&\quad \times \left(\frac{\hat{E}_{i,j,k} - \hat{E}_{i-1,j,k}}{\lambda} + \tilde{E}^{-}_{i-1/2,j,k} - \tilde{E}^{-}_{i+1/2,j,k}, \tilde{E}^{+}_{i+1/2,j,k} - \tilde{E}^{-}_{i+1/2,j,k} \right)
\end{aligned} \tag{24}$$

where $\lambda = \Delta t/\Delta x$, and φ_i is the discontinuity indicator, with its value between 0 and 1, and is defined by

$$\varphi_i = \frac{\beta_i}{\beta_i + \gamma_i} \tag{25}$$

where

$$\begin{aligned}
\beta_i = \left(\frac{\alpha_i}{\alpha_{i-1}} + \frac{\alpha_{i+1}}{\alpha_{i+2}} \right)^2 \qquad \gamma_i = \frac{|\hat{E}_{i\max} - \hat{E}_{i\min}|^2}{\alpha_i} \\
\alpha_i = (|\hat{E}_{i-1} - \hat{E}_i| + \varsigma)^2
\end{aligned} \tag{26}$$

with ς being a small positive number taken as 10^{-6}.

C. Time Discretization

An unfactored implicit scheme can be obtained from a nonlinear implicit scheme by linearizing the flux vectors about the previous time step and dropping terms of the second and higher order:

$$\left[I + \frac{\Delta t}{V}(\delta_\xi \hat{A} + \delta_\eta \hat{B} + \delta_\zeta \hat{C})\right][I - \Delta t \hat{D}]\Delta Q_{i,j,k}$$
$$= -\frac{\Delta t}{V}[(\tilde{E} - \tilde{E}_v)^n_{i+1/2,j,k} - (\tilde{E} - \tilde{E}_v)^n_{i-1/2,j,k}]$$
$$- \frac{\Delta t}{V}[(\tilde{F} - \tilde{F}_v)^n_{i,j+1/2,k} - (\tilde{F} - \tilde{F}_v)^n_{i,j-1/2,k}]$$
$$- \frac{\Delta t}{V}[(\tilde{G} - \tilde{G}_v)^n_{i,j,k+1/2} - (\tilde{G} - \tilde{G}_V)^n_{i,j,k-1/2}]$$
$$+ \Delta t H_{i,j,k} \equiv \text{RHS} \tag{27}$$

where I is the identity matrix; n is the time level; δ_ξ, δ_η, and δ_ζ are the difference operators; $\hat{A}$, $\hat{B}$, and $\hat{C}$ are the Jacobian matrices; $\hat{D} = \partial H/\partial Q$; and $\Delta Q = Q^{n+1} - Q^n$ is the increment of conservative variables. Note that the viscous terms are treated explicitly and the turbulent source functions are treated implicitly. Because the production term is positive, its linearization is not possible; however, there is a strong coupling between the flowfield, turbulent viscosity, and production term.

The matrix inversion resulting from the source-term linearization is performed before the spatial sweeps:

$$\left[I + \frac{\Delta t}{V}(\delta_\xi \hat{A} + \delta_\eta \hat{B} + \delta_\zeta \hat{C})\right]\Delta Q_{i,j,k} = (I - \Delta t \hat{D})^{-1}\text{RHS} \equiv \text{RHS}^* \tag{28}$$

The lower–upper symmetric-Gauss–Seidel (LU-SGS) implicit factorization scheme of Yoon and Jameson [28] and Yoon and Kwak [29,30] for Eq. (28) can be derived by combining the advantages of LU factorization and SGS relaxation. The LU-SGS scheme can be written as

$$LD^{-1}U\Delta Q = \text{RHS}^* \tag{29}$$

where

$$L = I + \frac{\Delta t}{V}(\delta_\xi^- \hat{A}^+ + \delta_\eta^- \hat{B}^+ + \delta_\zeta^- \hat{C}^+ - \hat{A}^- - \hat{B}^- - \hat{C}^-)$$
$$D = I + \frac{\Delta t}{V}(\hat{A}^+ - \hat{A}^- + \hat{B}^+ - \hat{B}^- + \hat{C}^+ - \hat{C}^-)$$
$$U = I + \frac{\Delta t}{V}(\delta_\xi^+ \hat{A}^- + \delta_\eta^+ \hat{B}^- + \delta_\zeta^+ \hat{C}^- + \hat{A}^+ + \hat{B}^+ + \hat{C}^+) \tag{30}$$

and δ_ξ^-, δ_η^-, and δ_ζ^- are backward-difference operators, and δ_ξ^+, δ_η^+, and δ_ζ^+ are forward-difference operators. Split Jacobian matrices of the flux vectors are constructed so that the eigenvalues of + matrices are nonnegative and those of − matrices are nonpositive; that is,

$$\hat{A}^\pm = R_\xi(\Lambda_\xi^\pm \pm \upsilon_\xi I)R_\xi^{-1} \qquad \hat{B}^\pm = R_\eta(\Lambda_\eta^\pm \pm \upsilon_\eta I)R_\eta^{-1}$$
$$\hat{C}^\pm = R_\zeta(\Lambda_\zeta^\pm \pm \upsilon_\zeta I)R_\zeta^{-1} \tag{31}$$

where R_ξ and R_ξ^{-1} are similarity transformation matrices of the eigenvectors of $\hat{A}$, and υ_ξ is a viscous corrected term defined as [31]. The Jacobian matrices $\hat{A}^\pm_{i+1/2,j,k}$ are computed using the Roe-averaged state between $Q_{i+1,j,k}$ and $Q_{i,j,k}$ and the area vectors at cell interface $(i + 1/2, j, k)$. Equation (29) can be inverted in three steps:

$$\Delta Q^* = L^{-1}\text{RHS}^* \tag{32a}$$

$$\Delta Q^{**} = D\Delta Q^* \tag{32b}$$

$$\Delta Q = U^{-1}\Delta Q^{**} \tag{32c}$$

D. Boundary Conditions

The mean flow and turbulent transport equations presented in the preceding sections represent an initial-boundary-value problem. To solve these equations, it is necessary to impose initial and boundary conditions. A uniform flowfield is chosen as the initial conditions for the mean flow equations. A uniform value of $\nu_t \approx 1000$ is set as the initial guess.

The boundary conditions of mean flow are set as follows:

1) No-slip boundary conditions for velocities are adopted on the solid surface, which is assumed to be an adiabatic wall.

2) The density and pressure on the wall are set to be equal to the values of the node points next to the wall. This gives first-order accuracy at the wall.

3) In the far field, a locally-one-dimensional characteristic type of boundary condition is used. For the turbulent transport equation, a zeroth-order extrapolation is used to specify conditions at the far field.

IV. Results and Discussion

Presented here are the results of two different 2-D turbulent flows and one 3-D turbulent flow computations to illustrate and test the codes. The two-dimensional cases are the transonic turbulent flows over NACA 0012 and RAE 2822 airfoils, respectively. The three-dimensional case is a transonic turbulent flow over an ONERA M6 wing. We compare our results with available experimental data and other computational results for each case. The accuracy and convergence rates of steady-state calculation of the original WENO5 and antidiffusive WENO5 schemes are compared. The effects of antidiffusive flux on resolution of contact discontinuities are examined. To save space, we shall denote the WENO5 ($r = 3$)

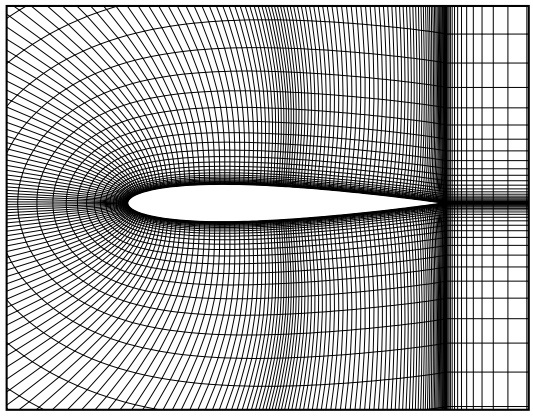

Fig. 1 C-type grid for a NACA 0012 airfoil.

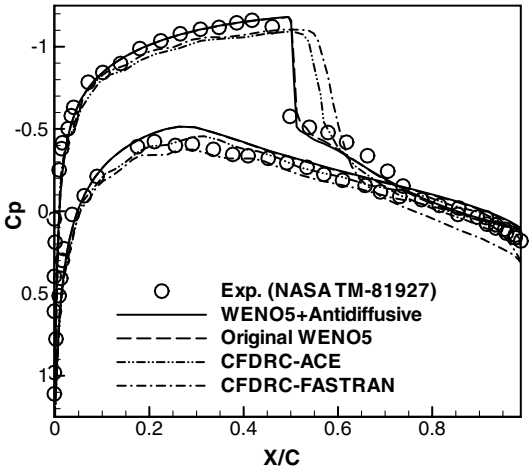

Fig. 2 A comparison of a NACA 0012 airfoil surface pressure distribution at $M_\infty = 0.799$, $\alpha = 2.26$ deg, and $Re_c = 9 \times 10^6$.

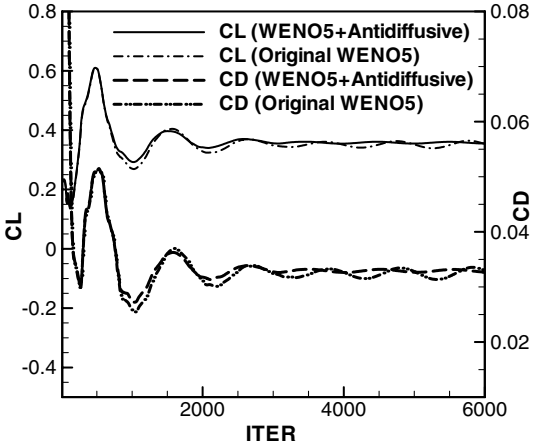

Fig. 3 Convergence of lift and drag coefficients of a NACA 0012 airfoil at $M_\infty = 0.799$, $\alpha = 2.26$ deg, and $Re_c = 9 \times 10^6$.

scheme with Roe's first-order flux as WENO5-R and the corresponding WENO5 ($r = 3$) scheme with Roe's first-order flux and antidiffusive flux as WENO5-R-AD in the following.

A. Flow over a NACA 0012 Airfoil

The first result is the transonic flow over a NACA 0012 airfoil at freestream conditions $M_\infty = 0.799$, $\alpha = 2.26$ deg, and $Re_c = 9 \times 10^6$. The angle of attack (2.26 deg) used in the computation is

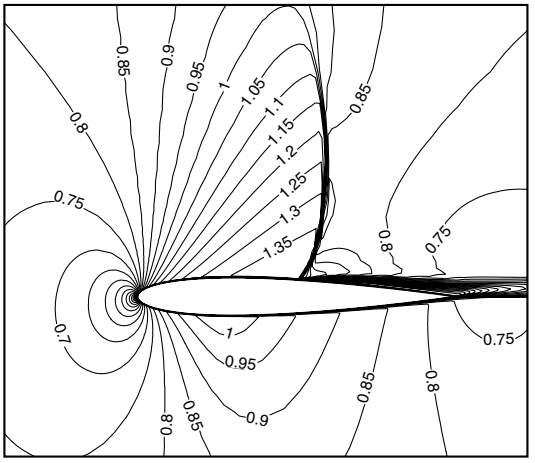

Fig. 4 Mach number contours for a NACA 0012 airfoil at $M_\infty = 0.799$, $\alpha = 2.26$ deg, and $Re_c = 9 \times 10^6$; WENO5-Roe scheme with antidiffusive flux corrections.

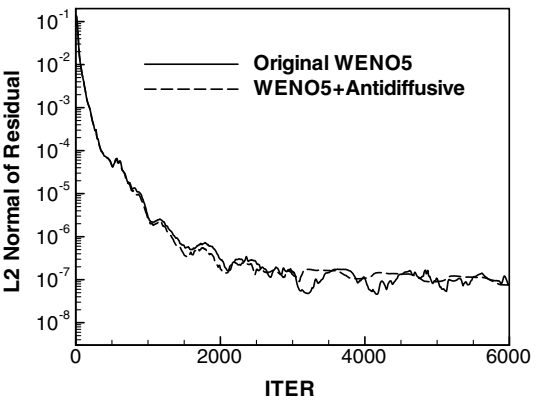

Fig. 5 Convergence history for a NACA 0012 airfoil at $M_\infty = 0.799$, $\alpha = 2.26$ deg, and $Re_c = 9 \times 10^6$.

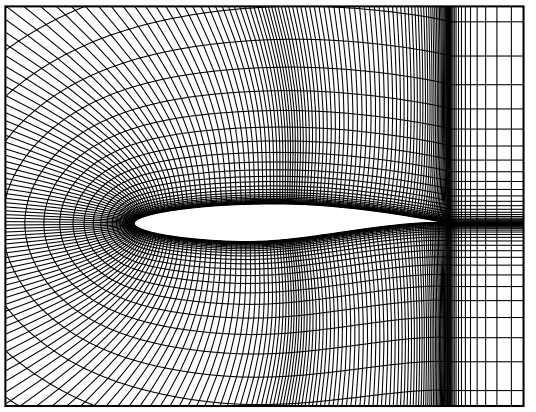

Fig. 6 C-type grid for a RAE 2822 airfoil.

obtained from the measured angle of attack (2.86 deg) using a linear wind-tunnel-wall correction procedure. For this transonic flowfield, a shock wave exists on the airfoil upper surface at about $x/c = 0.5$, which is strong enough to cause significant boundary-layer separation. This case represents a severe test for all solution methods in terms of both numerical algorithm as well as turbulence models.

To compare present results with computations from CFDRC-FASTRAN and CFDRC-ACE [32], a C-grid topology similar to that used in [32] was employed to model the NACA 0012 geometry. The airfoil was modeled using two domains: one domain for the airfoil and the other for the wake. The grid system, as shown in Fig. 1, has

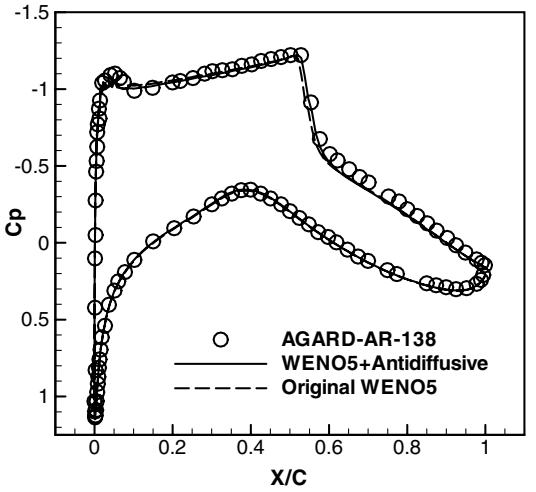

Fig. 7 Comparison of RAE 2822 airfoil surface pressure distribution at $M_\infty = 0.731$, $\alpha = 2.51$ deg, and $Re_c = 6.5 \times 10^6$.

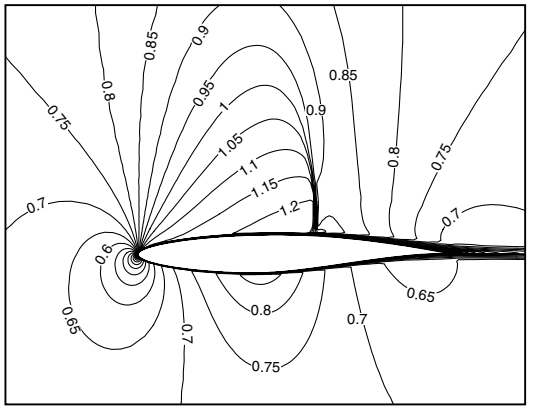

Fig. 8 Mach number contours for a RAE 2822 airfoil at $M_\infty = 0.731$, $\alpha = 2.51$ deg, and $Re_c = 6.5 \times 10^6$; WENO5-Roe scheme with antidiffusive flux corrections.

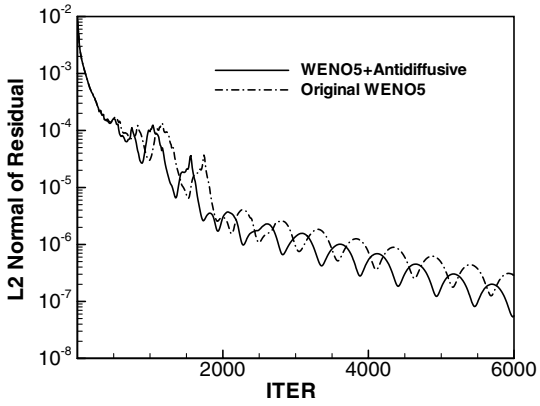

Fig. 9 Convergence history for a RAE 2822 airfoil at $M_\infty = 0.731$, $\alpha = 2.51$ deg, and $Re_c = 6.5 \times 10^6$.

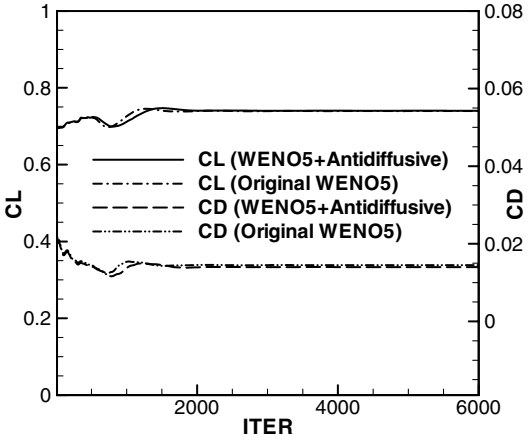

Fig. 10 Convergence of lift and drag coefficients of a RAE 2822 airfoil at $M_\infty = 0.731$, $\alpha = 2.51$ deg, and $Re_c = 6.5 \times 10^6$.

121 points on both the upper and lower surfaces of the airfoil, with 31 points normal to the airfoil surface. This grid distribution contains two domains with grid sizes of 241×31 and 61×61, respectively. The grid system extends from the airfoil surface to a circle of the far-field boundary located at approximately 50 chord lengths from the body. The first grid line is at a distance of 7×10^{-6} chord lengths off the wall, which resulted in a minimum of $y^+ < 1.5$ over the entire grid (here, $y^+ = u_\tau y/\nu$, where u_τ is the friction velocity).

The solutions were calculated using the original WENO5-R scheme and WENO5-R-AD scheme. Figure 2 shows the comparison of surface pressure distributions with the experimental data [33] and results of CFDRC-FASTRAN and CFDRC-ACE. Our computed results show that the upper-surface pressure is in better agreement with experimental data than that from CFDRC-FASTRAN and CFDRC-ACE, except for a slight discrepancy in the magnitude of lower-surface pressure. Both results of CFDRC-FASTRAN and CFDRC-ACE fail to predict the correct shock location. Computed lift and drag coefficients using the WENO5-R-AD scheme are $C_L = 0.355$ and $C_D = 0.0327$, respectively. The lift and drag coefficients of the original WENO5-R scheme are $C_L = 0.354$ and $C_D = 0.0335$. A slightly better C_L/C_D ratio can be achieved by the WENO5-R-AD scheme. The experimental values of lift and drag coefficients given by Harris [33] are $C_L = 0.391$ and $C_D = 0.033$. Figure 3 shows the convergence of lift and drag coefficients using the original WENO5-R and WENO5-R-AD schemes. Figure 4 shows the contours of constant-Mach-number contours using the WENO5-R-AD scheme. All the flow features are clearly resolved, including the front leading-edge structure, supersonic pocket, and shock separation. Figure 5 shows the convergence history for these two schemes. They display similar convergence patterns. A residual of 10^{-7} can be reached in about 6000 steps using both the original WENO5-R scheme and WENO5-R-AD. In general, they demonstrate the good convergence property in our implicit finite volume methods.

B. Flow over a RAE 2822 Airfoil

The next computation is for the transonic flow over a RAE 2822 airfoil, which has been tested extensively by Cook et al. [34]. This airfoil is a supercritical airfoil with a significant amount of aft camber. Solutions were obtained for this case on C-type meshes consisting of two domains: one domain for the airfoil and the other for the wake. The grid system has 121 points on both the upper and lower surfaces of the airfoil, with 31 points normal to the airfoil surface. This grid distribution produced two domains with dimensions of 241×31 and 61×61, respectively. The grid system, as shown in Fig. 6, is similar to that used in the NACA 0012 airfoil test case.

The result is for the transonic flow over a RAE 2822 airfoil at freestream condition $M_\infty = 0.725$, angle of attack $\alpha = 2.92$ deg, and reference Reynolds number based on airfoil chord, $Re_c = 6.5 \times 10^6$, corresponding to case 6 in the experimental study of Cook et al. [34]. Because of the presence of wall interference effects in the experiment, the corrected flow conditions with $M_\infty = 0.731$ and $\alpha = 2.51$ as suggested by Tatsumi et al. [35] are used. This flow involves a strong shock wave at $x/c = 0.55$ on the upper surface. The lift coefficient in this case depends strongly on the predicted shock location. This requires a good resolution of the shock wave. Jiang et al. [36] computed this problem using a convective upwind split pressure scheme with a Baldwin–Barth one-equation turbulence model.

In Fig. 7, the computed pressure coefficient distributions of the original WENO5-R and WENO5-R-AD are shown and compared with the experiment. The present results are in close agreement with

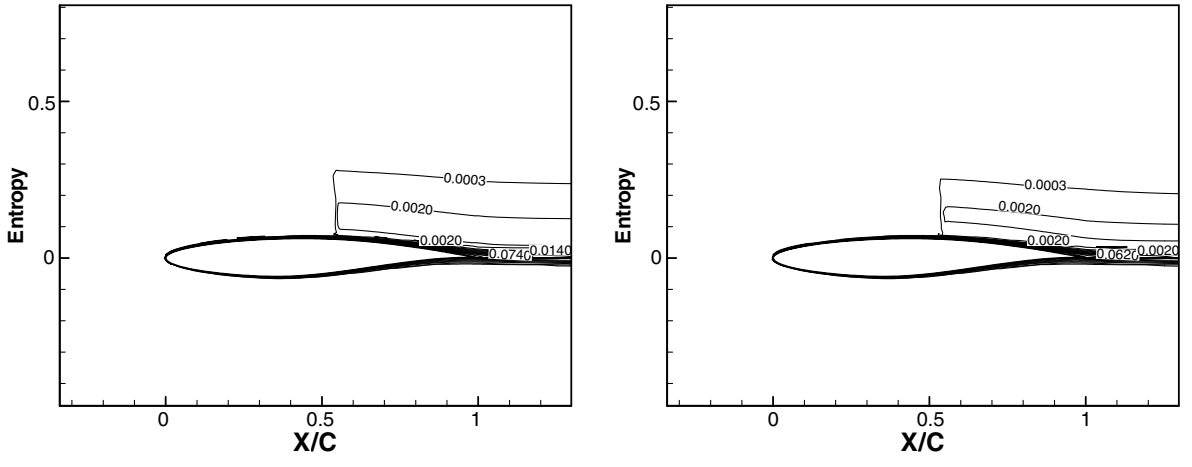

Fig. 11 Comparison of entropy contours of a RAE 2822 airfoil: a) original WENO5-Roe scheme and b) WENO5-Roe with antidiffusive flux.

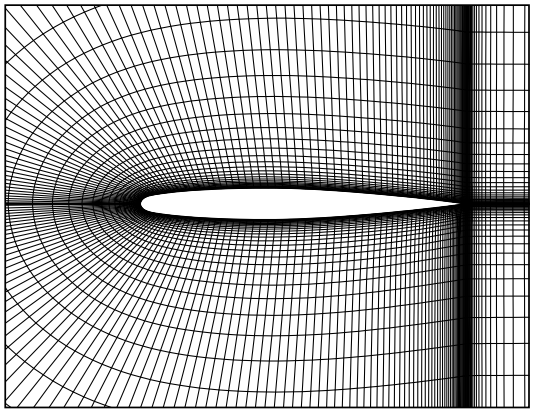

Fig. 12 C-type grid for an ONERA M6 wing at the symmetrical ($j = 1$) plane.

experimental data in all aspects. Figure 8 shows the contours of constant Mach numbers using the WENO5-Roe scheme with antidiffusive flux corrections. All the flow features are clearly resolved, including the front leading-edge structure, supersonic pocket, and shock separation. Figure 9 shows the convergence history, and it can be seen that the WENO5-R-AD scheme gives a better convergence rate in this RAE–2822 airfoil case. The computed lift and drag coefficients of the WENO5-R-AD scheme are $C_L = 0.740$ and $C_D = 0.0140$, whereas those by the WENO5-R scheme are $C_L = 0.740$ and $C_D = 0.0145$, respectively. Again, a slightly better C_L/C_D ratio can be obtained by the WENO5-R-AD scheme. The experimental values of lift and drag coefficients given by AGARD are $C_L = 0.743$ and $C_D = 0.0127$. Figure 10 shows the convergence of lift and drag coefficients using the WENO5-R and WENO5-R-AD schemes. A comparison of the entropy contours using WENO5-R and WENO5- R-AD is given in Fig. 11. Note that a noticeable difference in entropy production can be observed near the trailing edge for the antidiffusive WENO methods.

Our computed results for both the NACA 0012 and RAE 2822 airfoils are consistent with those given in the extensive compendium of results by Holst [37].

C. Three-Dimensional Transonic Flow over an ONERA M6 Wing

The result of three-dimensional case is the transonic flow over a ONERA M6 wing at $M_\infty = 0.8395$, with a 3.06 deg angle of attack and a reference Reynolds number $Re_c = 2.6 \times 10^6$. The ONERA M6 wing is a symmetric airfoil section with a sweep angle of 30 deg. The wing is tapered with a taper ratio of 0.56 and has an aspect ratio of 3.8. Extensive wind-tunnel-test data exist for the ONERA M6 wing: in particular, the pressure data for transonic flow conditions [38]. Takakura et al. [39] computed this problem using the Harten–Yee TVD scheme together with the Jones–Launder k-ε model. For comparison with results from CFDRC-FASTRAN [32], a C-grid topology similar to that used in [32] was employed to model

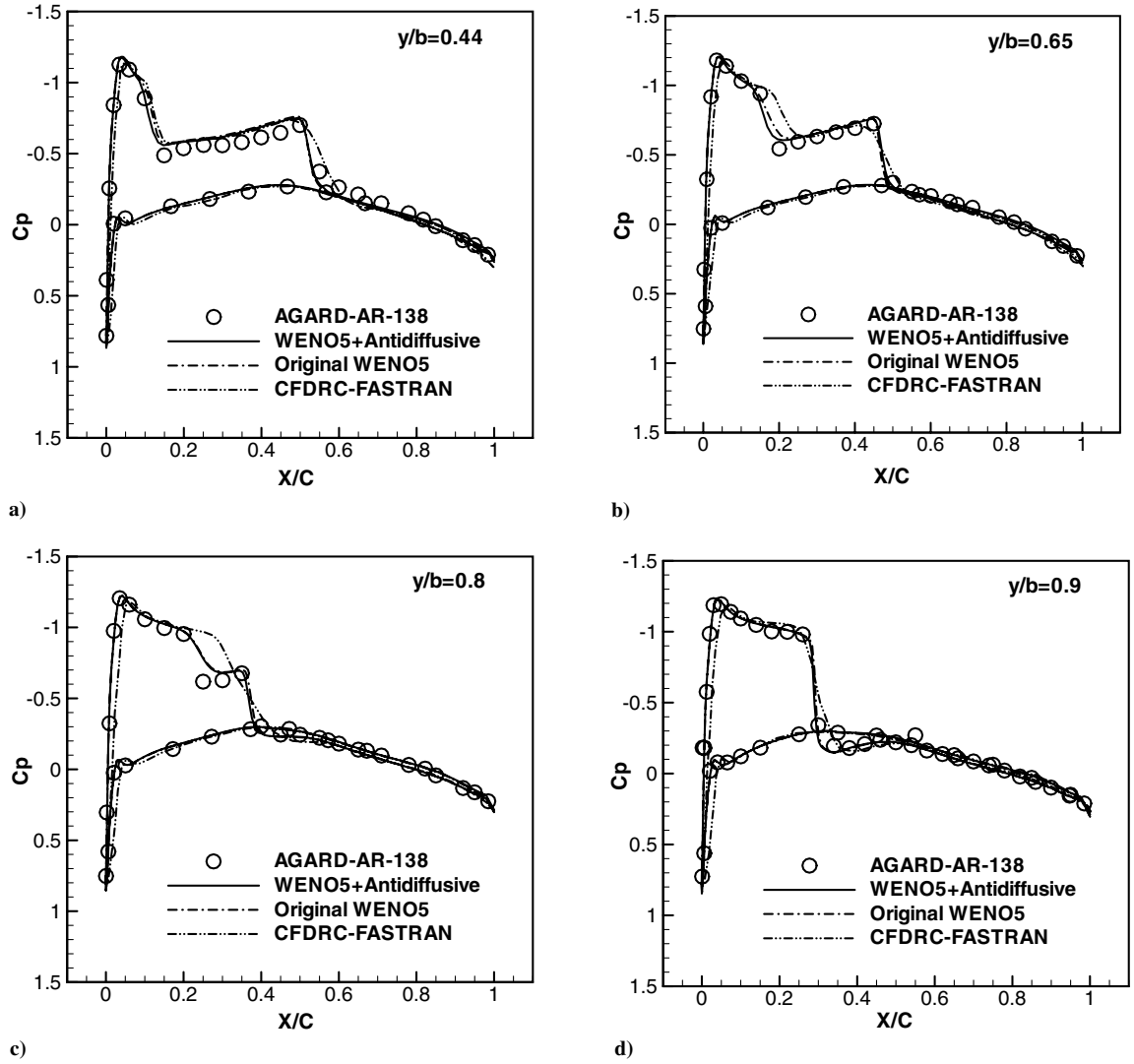

Fig. 13 Steady pressure distributions for an ONERA M6 wing at $M_\infty = 0.8395$, $\alpha = 3.06$ deg, and $Re_c = 2.6 \times 10^6$: a) $y/b = 0.44$, b) $y/b = 0.65$, c) $y/b = 0.80$, and d) $y/b = 0.90$.

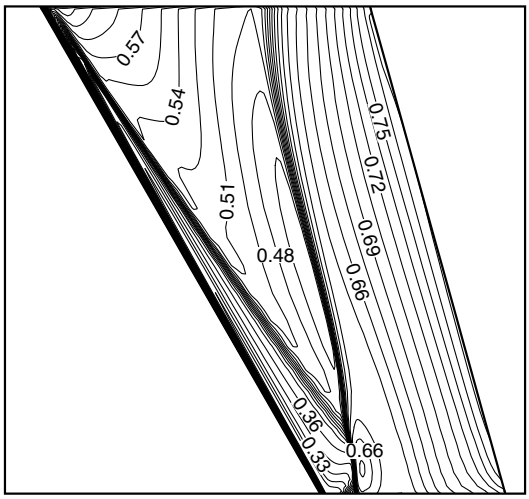

Fig. 14 Upper-surface pressure contours for an ONERA M6 wing at $M_\infty = 0.8395$, $\alpha = 3.06$ deg, and $Re_c = 2.6 \times 10^6$.

the ONERA M6 wing geometry. The airfoil was modeled using two domains: one domain for the upper surface and upper wake, with the grid dimension of $97 \times 49 \times 41$, and the other domain for the lower surface and lower wake, with the grid dimension of $97 \times 49 \times 41$. The outer boundaries were extended to 50 chord lengths in all directions of the mesh system. The first grid line is at a distance of 10^{-5} chord lengths off the wall, which resulted in a minimum of $y^+ < 2.0$ over the entire grid. The grid system was generated by letting the $j = 1$ plane (see Fig. 12) be the plane of grid points on the upper wing surface at the root section. The j planes were then distributed by power law along the upper surface to $j = 33$ at the upper-surface tip. Planes 34 through 41 were then rotated in a circular arc to model the wing tip. This wraparound wing tip allows the modeling of the wing tip as it existed in the wind-tunnel model.

The solutions were calculated using WENO5-R and WENO5-R-AD schemes. In Fig. 13, we show the surface pressure coefficients of the present results and compare them with experimental data [33] and other computations using CFDRC-FASTRAN. It is shown that our numerical results are in good agreement with the experimental data and are more accurate than the results of CFDRC-FASTRAN. This test case is at transonic condition and results in a double-shock configuration, which is evident in Figs. 13a–13c. Finally, Fig. 13d shows the shocks having coalesced to form one at the quarter-chord position, and this shock is by far the strongest shock of all those observed in Fig. 12. The configuration obviously results in the lambda double-shock pattern for transonic conditions on a swept wing. Among the three computational results, the WENO5-R-AD gives the best agreement with the experimental data. Figure 14 shows the pressure contours along the upper surface, and the double-shock pattern coalescing into a single shock at the tip can be observed. Figure 15 shows the convergence history; it indicates that in this case, the WENO5-R-AD gives a better convergence property than the original WENO5-R.

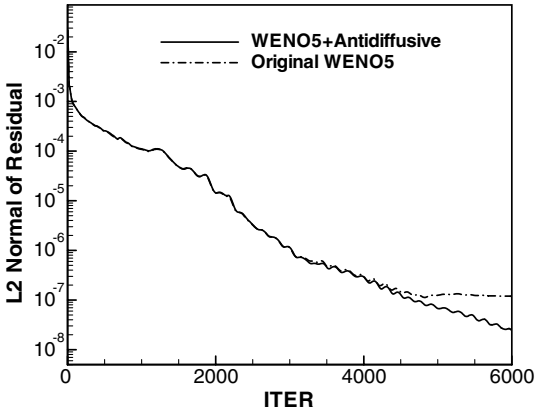

Fig. 15 Convergence history for an ONERA M6 wing at $M_\infty = 0.8395$, $\alpha = 3.06$ deg, and $Re_c = 2.6 \times 10^6$; WENO5 scheme.

V. Conclusions

Implicit WENO high-resolution numerical codes for solving the two- and three-dimensional compressible Navier–Stokes equations with the Spalart–Allmaras one-equation turbulence model have been developed. The present method adopts a numerical flux in flux-limiter form for the weighted essentially nonoscillatory spatial operator for convective flux, which allows for a more flexible choice to implement various first-order entropy-satisfying dissipative schemes. The integration of equations is via the implicit LU-SGS algorithm. Applications to turbulent transonic flows over NACA 0012 and RAE 2822 airfoils and three-dimensional turbulent flow over the ONERA M6 wing have been carried out to validate and illustrate the codes. The use of an implicit WENO5 scheme with antidiffusive flux corrections indicates better resolution of contact-discontinuity-related flow structures and a good convergence rate of steady-state computation as compared with that using the original WENO5-Roe scheme. It is found that for all the cases computed, the solutions including C_P, C_L, and C_D of the present algorithms are in good agreement with the experimental data and other available computational results. Furthermore, for the two-dimensional airfoil flow computations, smaller entropy production and a better C_L/C_D ratio can be found when antidiffusive WENO methods are employed. Thus, the present implicit antidiffusive WENO schemes, which have been tested in the compressible Euler [22] and Navier–Stokes equations, may lead to better resolution of contact-discontinuity-related flow features and their consequent evolution and may thus improve the computation of aerodynamic characteristics (e.g., C_L/C_D ratio).

Acknowledgments

This work was done under the auspices of the National Science Council of Taiwan through grant NSC-95-2212-E002-055. We thank Yeu-Ching Perng, Shih-Chang Yang, Horng-Tsair Lee, and Herng Lin of the Chung-Shan Institute of Science and Technology for many useful discussions.

References

[1] Harten, A., Engquist, B., Osher, S., and Chakravarthy, S., "Uniformly High-Order Accurate Nonoscillatory Scheme, 3," *Journal of Computational Physics*, Vol. 71, No. 2, 1987, pp. 231–303. doi:10.1016/0021-9991(87)90031-3

[2] Shu, C. W., and Osher, S., "Efficient Implementation of Nonoscillatory Shock Capturing Schemes," *Journal of Computational Physics*, Vol. 77, No. 2, 1988, pp. 439–471. doi:10.1016/0021-9991(88)90177-5

[3] Shu, C. W., and Osher, S., "Efficient Implementation of Nonoscillatory Shock Capturing Schemes, 2," *Journal of Computational Physics*, Vol. 83, No. 1, 1989, pp. 32–78. doi:10.1016/0021-9991(89)90222-2

[4] Cockburn, B., Johnson, C., Shu, C. W., and Tadmor, E., "Advanced Numerical Approximation of Hyperbolic Equations," *Lecture Notes in Mathematics*, edited by A. Quarteroni, Vol. 1697, Springer, New York, 1998, pp. 325–432.

[5] Yee, H. C., and Harten, A., "Implicit TVD Schemes for Hyperbolic Conservation Laws in Curvilinear Coordinates," *AIAA Journal*, Vol. 25, No. 2, 1987, pp. 266–274. doi:10.2514/3.9617

[6] Harten, A., "A High-Resolution Scheme for the Computation of Weak Solutions of Hyperbolic Conservation Laws," *Journal of Computational Physics*, Vol. 49, No. 3, 1983, pp. 357–393. doi:10.1016/0021-9991(83)90136-5

[7] Rogerson, A. M., and Meiburg, E., "A Numerical Study of the Convergence Properties of ENO Schemes," *Journal of Scientific Computing*, Vol. 5, No. 2, 1990, pp. 151–167. doi:10.1007/BF01065582

[8] Shu, C. W., "Numerical Experiments on the Accuracy of ENO and Modified ENO Schemes," *Journal of Scientific Computing*, Vol. 5,

No. 2, 1990, pp. 127–149.
doi:10.1007/BF01065581

[9] Casper, J., Shu, C. W., and Atkins, H., "Comparison of Two Formulations for High-Order Accurate Essentially Nonoscillatory Schemes," *AIAA Journal*, Vol. 32, No. 10, 1994, pp. 1970–1977.
doi:10.2514/3.12240

[10] Liu, X. D., Osher, S., and Chan, T., "Weighted Essentially Nonoscillatory Schemes," *Journal of Computational Physics*, Vol. 115, No. 1, 1994, pp. 200–212.

[11] Jiang, G. S., and Shu, C. W., "Efficient Implementation of Weighted ENO Schemes," *Journal of Computational Physics*, Vol. 126, No. 1, 1996, pp. 202–228.
doi:10.1006/jcph.1996.0130

[12] Chen, Y. N., Yang, S. C., and Yang, J. Y., "Implicit Weighted ENO Schemes for the Incompressible Navier–Stokes Equations," *International Journal for Numerical Methods in Fluids*, Vol. 31, No. 4, 1999, pp. 747–765.
doi:10.1002/(SICI)1097-0363(19991030)31:4<747::AID-FLD901>3.0.CO;2-F

[13] Yang, J. Y., Yang, S. C., Chen, Y. N., and Hsu, C. A., "Weighted ENO Schemes for the Three-Dimensional Incompressible Navier–Stokes Equations," *Journal of Computational Physics*, Vol. 146, No. 1, 1998, pp. 464–487.
doi:10.1006/jcph.1998.6062

[14] Perng, Y. C., Yen, R. H., and Yang, J. Y., "Implicit Weighted ENO Schemes for the Euler Equations," *Computational Fluid Dynamics Journal*, Vol. 8, No. 3, 1999, pp. 216–227.

[15] Yang, J. Y., Perng, Y. C., and Yen, R. H., "Implicit Weighted Essentially Non-Oscillatory Schemes for the Compressible Navier–Stokes Equations," *AIAA Journal*, Vol. 39, No. 11, 2001, pp. 2082–2090.
doi:10.2514/2.1231

[16] Despres, B., and Lagoutiere, F., "Contact Discontinuity Capturing Schemes for Linear Advection, Compressible Gas Dynamics," *Journal of Scientific Computing*, Vol. 16, No. 4, 2001, pp. 479–524.
doi:10.1023/A:1013298408777

[17] Bouchut, F., "An Anti-Diffusive Entropy Scheme for Monotone Scalar Conservation Law," *Journal of Scientific Computing*, Vol. 21, No. 1, 2004, pp. 1–30.
doi:10.1023/B:JOMP.0000027953.74841.8c

[18] Xu, Z., and Shu, C. W., "Anti-Diffusive Flux Corrections for High Order Finite Difference WENO Scheme," *Journal of Computational Physics*, Vol. 205, No. 2, 2005, pp. 458–485.
doi:10.1016/j.jcp.2004.11.014

[19] Henrick, A. K., Aslam, T. D., and Powers, J. M., "Mapped Weighted Essentially Non-Oscillatory Schemes," *Journal of Computational Physics*, Vol. 207, No. 2, 2005, pp. 542–567.
doi:10.1016/j.jcp.2005.01.023

[20] Zhang, S. H., and Shu, C. W., "A New Smoothness Indicator for the WENO Schemes and Its Effect on the Convergence to Steady State Solutions," *Journal of Scientific Computing*, Vol. 31, Nos. 1–2, 2007, pp. 273–305.
doi:10.1007/s10915-006-9111-y

[21] Roe, P., "Approximate Riemann Solvers, Parameter Vectors and Difference Schemes," *Journal of Computational Physics*, Vol. 43, No. 2, 1981, pp. 357–372.
doi:10.1016/0021-9991(81)90128-5

[22] Hsieh, T. J., Wang, C. H., and Yang, J. Y., "Numerical Experiments with Several Variant WENO Schemes for the Euler Equations," *International Journal for Numerical Methods in Fluids*, Vol. 58, Mar. 2008, pp. 1017–1039.
doi:10.1002/fld.1780

[23] Spalart, P. R., and Allmaras, S. R., "A One-Equation Turbulence Model for Aerodynamic Flows," AIAA Paper 92-0439, 1992.

[24] Spalart, P. R., and Allmaras, S. R., "A One-Equation Turbulence Model for Aerodynamic Flows," *La Recherche Aerospatiale: Bulletin Bimestriel de l'Office National d'Etudes et de Recherches Aerospatiales* No. 1, 1994, pp. 5–21.

[25] Bardina, J. E., Huang, P. G., and Coakley, T. J., "Turbulence Model Validation, Testing and Development," NASA TM-110446, Apr. 1997.

[26] Chakravathy, S. R., and Szema, K. Y., "An Euler Solver for Three-Dimensional Supersonic Flows with Subsonic Pockets," AIAA Paper 85-1703, 1985.

[27] Cinnella, P., and Grossman, B., in *Computational Methods in Hypersonic Aerodynamics*, edited by T. K. S. Murthy, Kluwer Academic, Norwell, MA, 1991, Chap. 5.

[28] Yoon, S., and Jameson, A., "Lower-Upper Symmetric-Gauss–Seidel Method for the Euler and Navier–Stokes Equations," *AIAA Journal*, Vol. 26, No. 9, 1988, pp. 1025–1026.
doi:10.2514/3.10007

[29] Yoon, S., and Kwak, D., "Three-Dimensional Incompressible Navier–Stokes Solver Using Lower-Upper Symmetric-Gauss–Seidel Algorithm," *AIAA Journal*, Vol. 29, No. 6, 1991, pp. 874–875.
doi:10.2514/3.10671

[30] Yoon, S., and Kwak, D., "Implicit Navier–Stokes Solver for Three-Dimensional Compressible Flow," *AIAA Journal*, Vol. 30, No. 11, 1992, pp. 2653–2658.
doi:10.2514/3.48957

[31] Coakley, T. J., "Turbulence Modeling Methods for the Compressible Navier–Stokes Equations," AIAA 16th Fluid and Plasma Dynamics Conference, AIAA Paper 83-1693, July 1983.

[32] CFDRC FASTRAN, Software Package, Ver. 2003, ESI Software, Huntsville, AL, 2003, Chap. 3.

[33] Harris, C. D., "Two-Dimensional Aerodynamic Characteristics of the NACA 0012 Airfoil in the Langley 8-Foot Transonic Pressure Tunnel," NASA TM-81927, 1981.

[34] Cook, P. H., McDonald, M. A., and Firmin, M. C. P., "Airfoil RAE 2822 Pressure Distributions and Boundary Layer and Wake Measurement," AGARD Rept. AR-138-A6, Neuilly-sur-Seine, France, 1979.

[35] Tatsumi, S., Martinelli, L., and Jameson, A., "A New High-Resolution Scheme for Compressible Flows Past Airfoil," AIAA Paper 95-0466, 1995.

[36] Jiang, Y. T., Damodaran, M., and Lee, K. H., "High Resolution Finite Volume Calculation of Turbulent Transonic Flow Past Airfoils," AIAA Paper 96-2377-CP, 1996.

[37] Holst, T. L., "Viscous Transonic Airfoil Workshop Compendium of Results," *Journal of Aircraft*, Vol. 25, No. 12, 1988, pp. 1073–1087.
doi:10.2514/3.45706

[38] Schimit, V., and Charpin, F., "Pressure Distributions on the ONERA M6 Wing at Transonic Mach Numbers," AGARD AR-138-B1, 1979.

[39] Takarura, Y., Ogawa, S., and Ishiguro, T., "Turbulence Models for 3-D Transonic Viscous Flows," AIAA Paper 89-1952-CP, 1989.

K. Powell
Associate Editor